

# Optical Properties of the Spin-Ladder Compound $\text{Sr}_{14}\text{Cu}_{24}\text{O}_{41}$

Z. V. Popović <sup>a</sup>, M. J. Konstantinović <sup>b</sup>, V. A. Ivanov <sup>a</sup>, O. P.

Khuong <sup>a</sup>, R. Gajić <sup>c</sup>, A. Vietkin <sup>d</sup> and V. V. Moshchalkov <sup>a</sup>

<sup>a</sup> *Laboratorium voor Vaste-Stoffysica en Magnetisme,*

*K. U. Leuven, Celestijnenlaan 200D, B-3001 Leuven, Belgium*

<sup>b</sup> *Max-Planck-Institut für Festkörperforschung,*

*Heisenbergstrasse 1, D-70569 Stuttgart, Germany*

<sup>c</sup> *Institute of Physics, P.O.Box 68, 11080 Belgrade, Yugoslavia and*

<sup>d</sup> *Physics Department, Moscow State University, 119899 Moscow, Russia*

## Abstract

We report the measurements of the pseudodielectric function, far-infrared reflectivity and Raman scattering spectra in  $\text{Sr}_{14}\text{Cu}_{24}\text{O}_{41}$  single crystal. We study the lattice and the spin dynamics of the  $\text{Cu}_2\text{O}_3$  spin ladders and  $\text{CuO}_2$  chains of this compound. The ellipsometric and the optical reflectivity measurements yield the gap values of 1.4 eV, 1.86 eV, 2.34 eV (2.5 eV) for the ladders (chains) along the **c**-axis and 2.4 eV along the **a**-axis. The electronic structure of the  $\text{Cu}_2\text{O}_3$  ladders is analyzed using tight-binding approach for the correlated electron systems. The correlation gap value of 1.4 eV is calculated with the transfer energy (hopping) parameters  $t = t_0 = 0.26$  eV, along and perpendicular to legs,  $t_{xy} = 0.026$  eV (interladder hopping) and  $U = 2.1$  eV, as a Coulomb repulsion. The optical parameters of the infrared active phonons and plasmons are obtained by oscillator fitting procedure of the reflectivity spectra. Raman scattering spectra are measured at different temperatures using different laser line energies. The two-magnon peak is observed at about  $2880 \text{ cm}^{-1}$ . At temperatures below 150 K the new infrared and Raman modes appear due to the charge ordering.

PACS numbers: 78.30.Hv; 78.20.Ci; 71.27.+a; 74.72.Jt

## I. INTRODUCTION

The  $\text{Sr}_{14}\text{Cu}_{24}\text{O}_{41}$  compound is one of the three stable phases in the Sr-Cu-O system which can be synthesized under ambient pressure. The other two stable phases are  $\text{Sr}_2\text{CuO}_3$ , which has simple chains of Cu ions, and  $\text{SrCuO}_2$  with zigzag chains of Cu ions. This oxide has unique crystal structure based on two sublattices; one of them consists of  $\text{Cu}_2\text{O}_3$  two-leg ladders and the second one is formed by  $\text{CuO}_2$  chains. These two sublattices are incompatible along one crystallographic direction, thus resulting in an 1D incommensurate structure [1]. According to the structural analysis [1], the ladder sublattice is face-centered-orthorhombic (space group  $Fmmm$ ) with a lattice parameters  $a=1.1459$  nm,  $b=1.3368$  nm and  $c_{\text{Ladder}}=0.3931$  nm. There are two ladder layers with two ladders per unit cell, Fig. 1. The chain sublattice is A-centered orthorhombic (space group  $Amma$ ), with nearly the same  $\mathbf{a}$  and  $\mathbf{b}$  axes but different  $\mathbf{c}$  axis,  $c_{\text{Chain}}=0.2749$  nm. However,  $\text{Sr}_{14}\text{Cu}_{24}\text{O}_{41}$  can be considered as nearly commensurate structure at  $7xc_{\text{Ladder}}=2.7372$  nm and  $10xc_{\text{Chain}}=2.7534$  nm. The schematic illustration of  $\text{Sr}_{14}\text{Cu}_{24}\text{O}_{41}$  crystal structure is given in Fig. 1.

The physical properties of  $\text{Sr}_{14}\text{Cu}_{24}\text{O}_{41}$  have attracted a lot of attention recently [2, 3, 4, 5, 6, 7, 8, 9, 10, 11, 12], in connection with the rich physics associated with the  $S=1/2$  Heisenberg antiferromagnetic quasi one-dimensional (1D) structures and the discovery of superconductivity in  $\text{Sr}_{0.4}\text{Ca}_{13.6}\text{Cu}_{24}\text{O}_{41}$  under high pressure [2]. The progress in this field has been summarized in Ref. [13]. Various magnetic [3, 4, 5], NMR [6, 7] and neutron scattering [8, 9] measurements, showed that  $\text{Sr}_{14}\text{Cu}_{24}\text{O}_{41}$  has two kinds of magnetic gaps. The first one,  $\Delta_L = 32.5$  meV, is attributed to the singlet-triplet excitation in the  $\text{Cu}_2\text{O}_3$  spin-ladders, with the exchange energies along the legs ( $J=130$  meV) and the rungs ( $J_0=72$  meV) [8]. The second one,  $\Delta_C = 11.5$  meV, is argued to arise from the spin dimer formation in the  $\text{CuO}_2$  chains [8], with an antiferromagnetic intradimer coupling  $J_1=11.2$  meV. Similar ratio of the superexchange interaction energies,  $J_0/J \sim 0.5$ , as well as the magnitude of  $J_0=(950\pm 300)$  K, is found in the  $^{17}\text{O}$  and  $^{63}\text{Cu}$  NMR measurements [6].

The Raman spectra of  $\text{Sr}_{14}\text{Cu}_{24}\text{O}_{41}$  were measured previously [14, 15]. From the comparison between Raman spectra of the various layered tetragonal cuprates, Abrashev *et al.* [14] concluded that the main contribution to the spectra comes from the Raman forbidden-infrared active LO phonons and the two-magnon scattering. Furthermore, Sugai *et al.* [15] argued that, besides strong two-magnon features, some low-frequency modes in the Ra-

man spectra are also magnetic in origin, since they have similar energies to those found in the neutron scattering experiments [8]. Still, for the proper identification of the magnetic modes, the temperature dependent Raman spectra, as well as the spectra in magnetic field, are required. Also, detailed analysis of the lattice dynamics and comparison between Raman and infrared (IR) spectra are indispensable due to the incommensurability of the structure. Therefore, we present here the Raman and IR spectra at various temperatures between 5 and 300 K in order to make more complete assignment of the vibrational modes in  $\text{Sr}_{14}\text{Cu}_{24}\text{O}_{41}$ . The Raman spectra are also measured under resonant conditions, with a laser light energy close to gap values. The correlated electron tight-binding model of electronic structure is used to estimate the hopping parameters, in fact adjusted to the measured gaps and exchange energies.

## II. EXPERIMENTAL DETAILS

The present work was performed on (010) oriented single crystal plates with dimensions typically about  $5 \times 1 \times 6 \text{ mm}^3$  in the **a**, **b** and **c** axes, respectively. The infrared measurements were carried out with a BOMEM DA-8 FIR spectrometer. A DTGS pyroelectric detector was used to cover the wave number region from 100 to  $700 \text{ cm}^{-1}$ ; a liquid nitrogen cooled HgCdTe detector was used from 500 to  $1500 \text{ cm}^{-1}$ . The spectra were collected with the  $2 \text{ cm}^{-1}$  resolution. The low temperature reflectivity spectra in the range from 30 to  $5000 \text{ cm}^{-1}$  were measured using Bruker IFS 133v FIR-spectrometer with Oxford-Cryostat. The Raman spectra were recorded in the backscattering configuration using micro- and macro-Raman systems with Dilor triple monochromator including liquid nitrogen cooled CCD-detector. An Ar- and Kr-ion lasers were used as an excitation source. We measured the pseudodielectric function with a help of a rotating-analyzer ellipsometer. We used a Xe-lamp as a light source, a double monochromator with 1200 lines/mm gratings and an S20 photomultiplier tube as a detector. The polarizer and analyzer were Rochon prisms. The measurements were performed in the 1.6-5.6 eV energy range. Optical reflectivity spectra were measured at room temperature in the 200-2000 nm spectral range using Perkin-Elmer Lambda 19 spectrophotometer.

### III. ELECTRONIC STRUCTURE

The electronic structure of  $\text{Sr}_{14}\text{Cu}_{24}\text{O}_{41}$  is calculated using the tight-binding method for correlated electrons [16]. Recent exact diagonalization and a variational Monte Carlo simulations revealed that electronic structure of  $\text{Sr}_{14}\text{Cu}_{24}\text{O}_{41}$  is well described by single ladder energy spectrum [17]. It means that electron energy dispersions are governed mainly by electrons in the ladder. According to the ARPES measurements [10], the chains contribute to the electronic structure of  $\text{Sr}_{14}\text{Cu}_{24}\text{O}_{41}$  with a dispersionless band. Without entering any lengthy discussions about the substance nonstoichiometry and the carrier transport between chains and ladders, we assume further on that the ladder unit  $\text{Cu}_2^{1+n}\text{O}_3^{2-}$  has total charge  $-2$ . In other words, there is one hole,  $n = 1$ , per copper ion in the ladder for negligibly small hybridization of its  $d_{x^2-y^2}$ -orbitals with the  $p_y$ -orbital of intermediate oxygens. The angle between Cu atoms of neighboring ladders is near right angle ( $88.7^\circ$ ), Fig. 1. In our consideration of the electronic structure we assumed that the directions between the nearest neighbor Cu ions form an ideal right angle.

The Hamiltonian for the correlated copper holes in the ladder with two rungs,  $a - b$  and  $c - d$ , per a unit cell can be written as

$$\begin{aligned}
 H = & -2t \sum_{p,\sigma} \cos p_y \left[ a_\sigma^+(p) a_\sigma(p) + b_\sigma^+(p) b_\sigma(p) + c_\sigma^+(p) c_\sigma(p) + d_\sigma^+(p) d_\sigma(p) \right] \\
 & -t_0 \sum_{p,\sigma} \left[ a_\sigma^+(p) b_\sigma(p) + c_\sigma^+(p) d_\sigma(p) + H.c. \right] \\
 & -t_{xy} \sum_{p,\sigma} \left[ e^{-i\sqrt{2}p_x} + e^{-i(\sqrt{2}p_x+p_y)} \right] \left[ a_\sigma^+(p) d_\sigma(p) + H.c. \right] \\
 & -t_{xy} \sum_{p,\sigma} \left( 1 + e^{-ip_y} \right) \left[ b_\sigma^+(p) c_\sigma(p) + H.c. \right] + U \sum_{i=a,b,c,d} n_{\uparrow i}^j n_{\downarrow i}^j - \mu \sum_{i=a,b,c,d} n_i^j,
 \end{aligned} \tag{1}$$

where  $a, b, c, d$  represent chains, (see Fig.1.(a)),  $t$  ( $t_0$ ) are the values of the carrier hopping along legs (rungs),  $t_{xy}$  is a hopping amplitude between ladders,  $U$  is the Anderson-Hubbard repulsion, and  $\mu$  is the chemical potential and other notations as usual. The  $x$  and  $y$  axis of the reference system are taken along the  $\mathbf{a}$  and the  $\mathbf{c}$  crystallographic directions, respectively. Applying the  $X$ -operator machinery [18], the correlation split energy bands are governed by zeros of the inverse Green's function in the first perturbation order with respect to tunneling

matrix:

$$\widehat{D}_p^{-1}(\omega) = \begin{pmatrix} A_{a-b} & B \\ B^* & A_{c-d} \end{pmatrix}, \quad (2)$$

where

$$\widehat{A}_{a-b} = \begin{matrix} a \{ \\ -2 \end{matrix} \begin{matrix} 0+ \\ -2 \end{matrix} \begin{pmatrix} \frac{-i\omega_n - \mu}{f_{0+}} + r & r & -t_0 & -t_0 \\ r & \frac{-i\omega_n - \mu + U}{f_{-2}} + r & -t_0 & -t_0 \\ -t_0 & -t_0 & \frac{-i\omega_n - \mu}{f_{0+}} + r & r \\ -t_0 & -t_0 & r & \frac{-i\omega_n - \mu + U}{f_{-2}} + r \end{pmatrix},$$

$$\widehat{B} = \begin{pmatrix} 0 & 0 & D & D \\ 0 & 0 & D & D \\ C & C & 0 & 0 \\ C & C & 0 & 0 \end{pmatrix}$$

$$\text{with } r = -2t \cos p_y, C = -t_{xy} (1 + e^{-ip_y}), D = -t_{xy} [e^{-i\sqrt{2}p_x} + e^{-i(\sqrt{2}p_x + p_y)}].$$

Here the correlation factors  $f_{0+}$ ,  $f_{-2}$  are determined by fermion occupation  $n$  per site. Namely, for the considered paramagnetic phase they are  $f_{0+} = 1 - n/2$ ,  $f_{-2} = n/2$  and all equal to  $1/2$  ( $n = 1$ ). After an analytical continuation,  $i\omega_n \rightarrow \xi + i\delta$ , in Eq.  $|\widehat{D}_p^{-1}(\omega)| = 0$  one can find the bonding /antibonding correlation energy dispersions as follows:

$$\xi_B^\pm(p) = \frac{1}{2} \left[ \varepsilon_p^{1,2} + \sqrt{(\varepsilon_p^{1,2})^2 + U^2} \right], \quad (3)$$

$$\xi_A^\pm(p) = \frac{1}{2} \left[ \varepsilon_p^{1,2} - \sqrt{(\varepsilon_p^{1,2})^2 + U^2} \right], \quad (4)$$

where  $\varepsilon_p^{1,2} = -2t \cos p_y \pm \sqrt{t_0^2 + (2t_{xy} \cos \frac{p_y}{2})^2} \pm 4t_0 t_{xy} \cos \frac{p_y}{2} \cos \frac{\sqrt{2}p_x}{2}$ .

For derivation of these energy dispersions from the eight-by-eight fold secular equation (see Eq.(2)) it was useful to apply the theorem about the decomposition of determinant with respect to diagonal elements (see Appendix A in Ref. [19]). The subbands  $\xi_B^-$  and  $\xi_A^-$  are completely occupied by carriers with concentration  $n = 1$  per copper site of ladder for the chosen chemical potential  $\mu = U/2$ . The nearest unoccupied energy band is  $\xi_B^+$  and the correlation gap in electronic structure can be estimated as

$$\Delta_{corr} = \min \xi_B^+(p) - \max \xi_A^-(p) = \quad (5)$$

$$\frac{1}{2} \left[ \sqrt{(t_0 + 2t - 2t_{xy})^2 + U^2} + \sqrt{(t_0 + 2t)^2 + U^2} \right] - (t_0 + 2t + t_{xy}).$$

For the dimensionless energies,  $\omega_p^{+,-} = \varepsilon_p^{1,2}/2t$ ,  $\tau_0 = t_0/2t$ ,  $\tau = t_{xy}/2t$ , the non-correlated electron density of states per spin,  $\rho(\varepsilon) = \sum_{p_x, p_y} [\delta(\varepsilon - \omega_p^+) + \delta(\varepsilon - \omega_p^-)]$ , for the unit cell volume, is defined analytically as follows

$$\begin{aligned} \rho_0^\alpha (-1 - 2\tau + \alpha\tau_0 \leq \varepsilon \leq -1 + 2\tau - \tau_0) &= \frac{4}{\pi^2 \sqrt{k_\alpha \tau}} K(q_\alpha), \\ \rho_0^\alpha \left( -1 + 2\tau + \alpha\tau_0 \leq \varepsilon \leq \frac{1}{2} + \tau + \alpha\tau_0 \right) &= \frac{4}{\pi^2 q_\alpha \sqrt{k_\alpha \tau}} F \left( \arcsin a_\alpha; \frac{1}{q_\alpha} \right), \\ \rho_0^\alpha (-1 + 2\tau + \alpha\tau_0 \leq \varepsilon \leq 1 + \alpha\tau_0) &= \frac{4}{\pi^2 q_\alpha \sqrt{k_\alpha \tau}} K \left( \frac{1}{q_\alpha} \right). \end{aligned} \quad (6)$$

Eqs.(6) represent the analytical expressions for the electron density of states via elliptic integrals  $F$  and  $K$  of the 1-st kind in the Legendre normal form with modulus  $q_\alpha = \sqrt{[2\tau(\tau + k_\alpha) + 1 - (\varepsilon + \alpha\tau_0)^2]}/k_\alpha\tau/2$ , argument  $a_\alpha = \sqrt{[2\tau(\tau + k_\alpha) + 1 - (\varepsilon + \alpha\tau_0)^2]}/[(1 + \varepsilon + \alpha\tau_0)(\tau + k_\alpha)k_\alpha]$ , where  $k_\alpha = \sqrt{\tau^2 + 2(1 - \varepsilon - \alpha\tau_0)}$  and  $\alpha = \pm$ .

The electron-electron repulsion,  $U$ , splits the density of the non-correlated electronic states  $\rho_0$ . The correlated electron density of states is

$$\begin{aligned} \rho(\varepsilon) &= \frac{2}{1 + \frac{\xi'_+}{\sqrt{(\xi'_+)^2 + (\frac{U}{2t})^2}}} \rho_0(\xi'_+) + \frac{2}{1 - \frac{\xi'_-}{\sqrt{(\xi'_-)^2 + (\frac{U}{2t})^2}}} \rho_0(\xi'_-), \text{ where} \\ \xi'_\pm &= \frac{\xi_\pm^2 - (\frac{U}{2t})^2}{\xi_\pm} + S \\ \text{and } S &= \frac{1}{4} \left[ \sqrt{(1 + 2\tau + \tau_0)^2 + \left(\frac{U}{t}\right)^2} - \sqrt{(1 + \tau_0)^2 + \left(\frac{U}{t}\right)^2} - 2\tau \right], \end{aligned} \quad (7)$$

are expressed via dimensionless correlated energies  $\xi_\pm \equiv \xi^\pm(p)/2t$ . With the help of Eq.(7) and Eqs.(6) one can calculate the correlated electron density of states for corresponding energy ranges. Its explicit form naturally includes the first kind elliptic integrals. The results of the calculations are plotted in Fig. 2.

The overlap of the energy ranges for the electronic dispersions, Eq.(3), leads to the special features of the correlated electronic structure at  $L_5 = 1/2(-1 - 2\tau + \tau_0) - S - 1/2\sqrt{(1 + 2\tau + \tau_0)^2 + (U/t)^2}$  and  $L_7 = 1/2(1/2 + \tau + \tau_0) - S - 1/2\sqrt{(1/2 + \tau + \tau_0)^2 + (U/t)^2}$

in the lower correlated band. Logarithmic divergencies inside the band at  $L_2 = 1/2(-1 + 2\tau - \tau_0) - S - 1/2\sqrt{(-1 + 2\tau - \tau_0)^2 + (U/t)^2}$ ,  $L_4 = 1/2(1 - \tau_0) - S - 1/2\sqrt{(1 - \tau_0)^2 + (U/t)^2}$ ,  $L_6 = 1/2(-1 + 2\tau + \tau_0) - S - 1/2\sqrt{(-1 + 2\tau + \tau_0)^2 + (U/t)^2}$  and at the correlated band edge  $L_8 = 1/2(1 + \tau_0) - S - 1/2\sqrt{(1 + \tau_0)^2 + (U/t)^2}$  are clear manifestations of the 2D electronic structure of  $\text{Sr}_{14}\text{Cu}_{24}\text{O}_{41}$  compound. We would like to emphasize that in the one-dimensional case ( $t_{xy} \rightarrow 0$ ) the electron density of states is taking features of a single spin-ladder without any logarithmic peaks, then the divergencies become square-root like and they are located at the band edges,  $\varepsilon = \pm 1$ :  $\rho(\varepsilon) = 8K(0)/\pi^2\sqrt{1 - \varepsilon^2} = 4/\pi\sqrt{1 - \varepsilon^2}$ .

#### IV. EXPERIMENTAL RESULTS

The dielectric function  $\epsilon_2$  of  $\text{Sr}_{14}\text{Cu}_{24}\text{O}_{41}$  is shown in Fig.3 in the spectral region from 1.6 eV to 5.5 eV. These spectra were computed from the measured Fourier coefficients using the equations for an isotropic case. Consequently,  $\epsilon_2$  represents a complicated average of the projections of the dielectric tensor on the sample surface. We presented the spectra of the (010) surface taken with the **a**-axis, Fig. 3(a) and **c** axis, Fig. 3(b), in the plane of incidence (PI). According to the prescription given by Aspnes [20], we attribute these components to the components of the dielectric tensor  $\epsilon_2^{aa}$  and  $\epsilon_2^{cc}$ . The bands with the energies of 2.4, 4.1, and 4.7 eV for the **a**-axis and at about 1.86, 2.34, 2.5, and 4.3 eV are found for the **c** axis in the plane of incidence, respectively.

Inset (a) in Fig. 3 shows reflectivity spectra of  $\text{Sr}_{14}\text{Cu}_{24}\text{O}_{41}$ . These spectra are calculated from measured dielectric functions  $\epsilon_1$  and  $\epsilon_2$ . Inset (b) in Fig. 3 represents the unpolarized optical reflectivity of  $\text{Sr}_{14}\text{Cu}_{24}\text{O}_{41}$  measured at room temperature. In addition to peaks, previously observed in ellipsometric measurements, a new peak at about 1.4 eV appears.

The room temperature polarized far-infrared reflectivity spectra of  $\text{Sr}_{14}\text{Cu}_{24}\text{O}_{41}$  are given in Fig. 4. The open circles are the experimental data and the solid lines represent the spectra computed using a four-parameter model for the dielectric constant:

$$\epsilon(\omega) = \epsilon_{\infty} \left( \prod_{j=1}^n \frac{\omega_{LO,j}^2 - \omega^2 + i\gamma_{LO,j}\omega}{\omega_{TO,j}^2 - \omega^2 + i\gamma_{TO,j}\omega} - \frac{\omega_p^2}{\omega(\omega - i\tau^{-1})} \right), \quad (8)$$

where  $\omega_{LO,j}$  and  $\omega_{TO,j}$  are longitudinal and transverse frequencies of the  $j^{\text{th}}$  oscillator,  $\gamma_{LO,j}$  and  $\gamma_{TO,j}$  are their corresponding dampings,  $\omega_p$  is the plasma frequency,  $\tau$  is the

free-carrier relaxation time and  $\epsilon_\infty$  is the high-frequency dielectric constant.

The best fit parameters are given in Table I. The agreement between observed and calculated reflectivity spectra is rather good. For the  $\mathbf{E}||\mathbf{a}$  polarization, eight oscillators with TO frequencies at about 164, 194, 219, 249, 283.5, 310.4, 554 and 623  $\text{cm}^{-1}$  are clearly seen. In the  $\mathbf{E}||\mathbf{c}$  polarization, Fig. 4(b), nine oscillators at 135, 148, 253, 293, 345, 486, 540, 596 and 620  $\text{cm}^{-1}$  are observed. Besides phonons, our model includes the Drude expression for light scattering on free carriers. We obtained the plasma frequency at about 4000  $\text{cm}^{-1}$  (1000  $\text{cm}^{-1}$ ) for the  $\mathbf{E}||\mathbf{c}$  ( $\mathbf{E}||\mathbf{a}$ ) polarizations.

The room temperature Raman spectra of  $\text{Sr}_{14}\text{Cu}_{24}\text{O}_{41}$ , for (aa) and (cc) polarized configurations are presented in Figs. 5(a) and 5(b). These spectra consist of only  $A_g$  symmetry modes. Four modes at 246, 302, 548, and 582  $\text{cm}^{-1}$  are clearly seen. The low temperature (cc) Raman spectra are given in Figs. 5(c)-(g). By lowering temperature below 200 K, the modes narrow and in addition the new modes appear. We will discuss them later on. The Raman spectra of  $\text{Sr}_{14}\text{Cu}_{24}\text{O}_{41}$ , excited by different lines of Ar and Kr lasers at 8 K, are shown in Fig. 6 for the (cc) and (aa) polarized configurations in the spectral ranges: (a) from 700 to 1400  $\text{cm}^{-1}$ , (b) from 1675 to 1975  $\text{cm}^{-1}$  and (c) from 2600 to 3300  $\text{cm}^{-1}$ . Anticipating our conclusions, we divide the Raman spectra in three different energy regions: one phonon (0-700  $\text{cm}^{-1}$ ), two-phonon (700-1400  $\text{cm}^{-1}$ ) and two-magnon region (above 1500  $\text{cm}^{-1}$ ). The mode at about 2900  $\text{cm}^{-1}$  and a broad structure at about 1900  $\text{cm}^{-1}$  are magnetic in origin, according to their intensity and frequency dependence as a function of the temperature, see Fig. 7.

## V. DISCUSSION

The average unit cell of  $\text{Sr}_{14}\text{Cu}_{24}\text{O}_{41}$  consists of four formula units with 316 atoms in all. Since there is a large number of atoms in the unit cell, we can expect a very large number of optically active modes. Consequently, the lattice dynamical calculation is practically impossible. All atoms have 4(e) position symmetry of  $Pcc2$  ( $C_{2v}^3$ ) space group [1]. Factor-group-analysis (FGA) yields the following distribution of vibrational modes:

$$\Gamma_{\text{Sr}_{14}\text{Cu}_{24}\text{O}_{41}} = 237A_1(\mathbf{E}||\mathbf{c}, aa, bb, cc) + 237A_2(ab) + 237B_1(\mathbf{E}||\mathbf{a}, ac) + 237B_2(\mathbf{E}||\mathbf{b}, bc) \quad (9)$$



According to this representation one can expect 948 modes which are both Raman and infrared active. Experimentally, the number of observed modes is less than ten for each polarization. Because of that, we consider separately the contribution of each sublattice unit. As mentioned earlier, the space group of ladder sublattice is  $Fm\bar{m}n$  ( $D_{2h}^{23}$ ). The site symmetries of Sr, Cu, O<sub>1</sub> and O<sub>2</sub> atoms are (8h), (8g), (8g) and (4b), respectively. The FGA for the ladder structure ( $\text{Sr}_2\text{Cu}_2\text{O}_3$ ) yields [21]:

$$\Gamma_{Ladder} = 3A_g + 3B_{1g} + 2B_{2g} + B_{3g} + 4B_{1u} + 4B_{2u} + 4B_{3u}$$

The space group of a chain sublattice is  $Amma$  ( $D_{2h}^{17}$ ). The site symmetries of Cu and O atoms are (4c) and (8f). The FGA gives for the chain structure:

$$\Gamma_{Chain} = 3A_g + 3B_{1g} + 2B_{2g} + B_{3g} + A_u + 2B_{1u} + 3B_{2u} + 3B_{3u},$$

Since  $Amma$  is not a standard setting for  $D_{2h}^{17}$  space group ( $Cmcm$ ) we use  $C_s^{xy}$  site symmetry for oxygen atoms and  $C_{2v}^x$  symmetry for Cu atoms in above representations. Thus, the total number of vibrational modes from both sub-units is:

$$\Gamma = 6A_g(aa, bb, cc) + 6B_{1g}(ab) + 4B_{2g}(ac) + 2B_{3g}(bc) + A_u + 6B_{1u}(\mathbf{E}||\mathbf{c}) + 7B_{2u}(\mathbf{E}||\mathbf{b}) + 7B_{3u}(\mathbf{E}||\mathbf{a}) \quad (10)$$

According to this analysis we should expect  $6A_g$  modes; one mode from vibrations of the Sr atoms, two modes which originate from vibrations of Cu atoms and other three  $A_g$  modes are due to oxygen vibrations. In order to assign the observed  $A_g$  modes we compare our spectra with the corresponding spectra of the Cu-O based materials with similar structural units as in  $\text{Sr}_{14}\text{Cu}_{24}\text{O}_{41}$ . For example, in  $\text{SrCuO}_2$  [22] and  $\text{YBa}_2\text{Cu}_4\text{O}_8$  [23] the Cu-O double layers exist and resemble the one leg of the ladder structure in  $\text{Sr}_{14}\text{Cu}_{24}\text{O}_{41}$ . The Cu-O chains, formed from copper oxide squares with the common edges, as in  $\text{Sr}_{14}\text{Cu}_{24}\text{O}_{41}$ , are also present in CuO [24] and  $\text{CuGeO}_3$  [25]. Thus, the lowest frequency mode in Fig. 5(a) at  $246 \text{ cm}^{-1}$  can be assigned to vibrations of the Cu ladder atoms (see Fig. 1). The corresponding  $A_g$  mode of copper vibrations in  $\text{YBa}_2\text{Cu}_4\text{O}_8$  ( $\text{SrCuO}_2$ ) appears at 250 (263)  $\text{cm}^{-1}$ . The next mode is found at  $302 \text{ cm}^{-1}$ . This mode represents the vibrations of the chain oxygen atoms along the  $\mathbf{a}$ -axis and appears in CuO at the same frequency [24]. The mode at  $548 \text{ cm}^{-1}$  is breathing mode of O<sub>1</sub> oxygen ladder atoms. Similar mode appears in  $\text{SrCuO}_2$  at  $543 \text{ cm}^{-1}$ . The second oxygen ladder atom (O<sub>2</sub>), Fig. 1, is situated in the center of inversion ( $D_{2h}$  site symmetry) and has no Raman activity. The highest frequency Raman mode in Figs. 5(a)-(b), at about  $582 \text{ cm}^{-1}$ , is caused by the chain oxygen vibrations along

the **c**-axis. Corresponding mode appears in CuO at  $633\text{ cm}^{-1}$  [24] and in CuGeO<sub>3</sub> at  $594\text{ cm}^{-1}$  [25]. The vibrations of Sr atoms, with frequency of  $188\text{ cm}^{-1}$  as in SrCuO<sub>2</sub>, are not observed in the spectra. Finally, the A<sub>g</sub> mode at  $153\text{ cm}^{-1}$ , see Fig. 8, originates from the vibrations of the Cu atom in chains. Again, similar mode is found in YBa<sub>2</sub>Cu<sub>4</sub>O<sub>8</sub> at  $153\text{ cm}^{-1}$ .

By lowering temperature Raman peaks narrow and at about T=150 K the new modes appear (Fig. 5 and Table II). Similar effects are found in the IR spectra as well. This temperature coincides with the charge ordering temperature established in the NMR and neutron scattering experiments [7, 9]. NMR study [7] showed the splitting of signal from Cu<sup>3+</sup> ions into two peaks below 200K suggesting the occurrence of the charge ordering. This effect is confirmed by Cox *et al.* [11]. They measured synchrotron x-ray scattering on Sr<sub>14</sub>Cu<sub>24</sub>O<sub>41</sub> single crystals and showed the appearance of the satellite peaks at (00l) positions. The results are interpreted in terms of a charge-ordered model involving both dimerization between two-nearest-neighbors of Cu<sup>2+</sup> ions surrounding a Cu<sup>3+</sup> ion on a Zhang-Rice singlet site, and dimerization between nearest-neighbors of Cu<sup>2+</sup> ions.

Fig. 8(a) shows the (cc) polarized low temperature (T=10 K) Raman spectra of Sr<sub>14</sub>Cu<sub>24</sub>O<sub>41</sub> in the  $125 - 750\text{ cm}^{-1}$  spectral region, excited with 647.1 nm (1.91 eV) and 488 nm (2.54 eV) energies. There are a remarkable difference between Raman spectra for these excitation lines which appears due to resonance effects. Namely, both lines are very close to gap energies for polarization along c-axis, see Fig. 3. The reflectivity spectra measured at 10 K for the **E**||**c** and the **E**||**a** polarizations are given in Figs. 8(b) and 8(c), respectively. In order to compare Raman with IR data we shown in the same figure the  $\epsilon_2(\omega)$  and the  $-Im[1/\epsilon(\omega)]$  spectra. These spectra are obtained using Kramers-Kronig analysis of reflectivity data. The TO and LO mode frequencies are obtained as peak positions of the  $\epsilon_2(\omega)$  and the  $-Im[1/\epsilon(\omega)]$ , respectively. For most of all Raman active modes we found theirs infrared counterparts (some of them are denoted by vertical lines) either for the **E**||**a** or the **E**||**c** polarizations. The appearance of similar lines in IR and Raman spectra, if not being the consequence of the symmetry, may also be attributed to the resonant conditions. It is well documented [26, 27] that Raman forbidden IR active LO modes appear in the Raman spectra of the insulating Cu-O based materials for the laser line energies close to gap values. The appearance of these modes in the Raman spectra is explained by Fröhlich interaction [26]. Here, since the 647.1 nm line is very close to the gap values (1.86 eV, see

Fig. 3) one can expect that the IR LO modes appear in the Raman spectra of  $\text{Sr}_{14}\text{Cu}_{24}\text{O}_{41}$  as well. Such effect is usually accompanied by the observation of the strong phonon overtones, as we shown in Fig. 6(a). All modes with energies higher than  $700\text{ cm}^{-1}$  are in fact the second order combinations (overtones) of the low-energy modes. The assignment and the frequencies of these modes are given in Table III. Therefore, the properties of the modes observed in our spectra may be understood in terms of the available symmetry combined with resonant effects, thus making proper identification of the low-temperature phonons practically impossible without detailed structural analysis.

Now we focus on magnetic properties. As it is mentioned earlier, the neutron scattering and NMR measurements estimated the spin-ladder gap value to be at  $\Delta_L = 32.5\text{ meV}$  ( $268\text{ cm}^{-1}$ ) [8] or at  $40.5\text{ meV}$  ( $326\text{ cm}^{-1}$ ) [28], respectively. Because of that, we paid special attention to the  $200\text{-}350\text{ cm}^{-1}$  spectral range, Fig. 5 (left panel). By lowering temperature we observe the appearance of the new modes at  $262$ ,  $293$ , and  $317\text{ cm}^{-1}$ . At the same time we find the modes with the same energy in the low-temperature IR spectra, Figs. 8(b)-(c). The  $262\text{ cm}^{-1}$  mode is very close in energy to the magnetic gap, thus possibly one-magnon excitation, as proposed by Sugai *et al.*[15]. However, the origin of the one-magnon excitation in the light scattering process usually comes from the spin-orbit interaction, which is found to be very small in transition metal oxides due to quenched orbital momentum of the transition metal ions. Moreover, below  $100\text{ K}$ , this mode has nearly the same temperature dependency of the frequency and intensity, like all other low-temperature modes and we identify them as zone edge phonons, which become Raman active due to the zone folding effect caused by the charge ordering transition [7]. Yet another type of magnetic excitations is expected to appear in the Raman spectra of two-leg-ladders at energies close to  $2\Delta_L \sim 534\text{ cm}^{-1}$  [29]. The mode at  $498\text{ cm}^{-1}$  (see Fig. 5 (g), right panel) shows a typical asymmetric shape with a tail towards high-frequencies, as expected for the onset of the two-magnon continuum. Its energy difference from  $2\Delta_L$  could be the magnon binding energy. However, as it is shown in Fig. 8(b), this mode is positioned between TO and LO frequencies of very strong IR active mode in the  $\mathbf{E}||\mathbf{c}$  spectra. This mode also shows a strong resonant enhancement, see Fig. 8 (a). Therefore, at this stage, it is hard to make definite conclusions about the origin of this mode and further experiments are needed to clarify this issue. Similar discussion holds for the spectral range around the twice the spin-gap value associated with a chains,  $2\Delta_C \sim 180\text{ cm}^{-1}$  [8], where continuum-like feature is also found in the Raman spectra.

Finally, we discuss the modes in the spectral range above  $1500 \text{ cm}^{-1}$ . The strongest mode in the spectra is centered at about  $2840 \text{ cm}^{-1}$  for the  $488 \text{ nm}$  excitation and at about  $2880 \text{ cm}^{-1}$  for the  $514.5 \text{ nm}$  excitation line. This feature decrease in intensity and shifts to lower energies at higher temperatures, Fig. 7. The same structure is already observed in many copper oxides at similar frequencies [27, 29]. Thus, all observed effects indicate the two-magnon origin of this mode. The energy of the two-magnon mode, associated with a top of the magnon brunch, in copper oxide insulators is about  $3J$ , where  $J$  represents the exchange interaction.

In the case of the two-leg-ladders, its energy position for different polarized configurations in the Raman spectra may be used to estimate the exchange parameters parallel ( $J$ ) and perpendicular ( $J_0$ ) to the ladders [30]. Since the energy position of the two-magnon peak is the same for (cc) and (aa) polarizations, Fig. 6(c), such an analysis suggests that  $J = J_0$ . This conclusion is fully in agreement with Raman scattering data of Ref.[15] and recent high-energy neutron scattering measurements[31], but inconsistent with previous neutron [8], NMR[6] and magnetization measurements, which estimated  $J_0/J$  ratio to be between 0.5 and 0.8. The discrepancy may be related to the fact that in the previous measurements, the high-energy magnetic excitations were not observed directly, but estimated indirectly from the low-energy spin gap measurements assuming an ideal model [32]. Thus, the Raman scattering is more direct method to obtain  $J_0/J$  ratio. The two-magnon mode at  $2880 \text{ cm}^{-1}$  gives exchange energy  $J=119 \text{ meV}$ , very close to the neutron scattering value  $J=130 \text{ meV}$  [8].

It is also interesting to note that the two-magnon mode is asymmetric with the spectral weight shifted to higher frequencies. Such a spectral shape of the two-magnon mode can be a consequence of the resonance [30], or it can be related to the bound-hole-pair effects [15]. Still, further experiments on the hole doped crystals are necessary to clarify this point.

Let us consider Fig. 6(b), where a weak structure appears in (cc) spectra at about  $1920 \text{ cm}^{-1}$ . Its energy is exactly equal to  $2J$  and varies with a laser line frequency in a similar way as the two-magnon mode at  $2880 \text{ cm}^{-1}$ . The energy shift of this mode as a function of temperature was not seen because of its very low intensity, thus leaving the origin of this mode as an open question. In addition to the  $1920 \text{ cm}^{-1}$  mode, we found a weak structure at about  $1700 \text{ cm}^{-1}$ , as well. This mode does not possess any noticeable temperature dependencies of energy and intensity. We concluded that this mode is an overtone phonon

mode. Its frequency can be represented as the third order of the  $568 \text{ cm}^{-1}$  mode ( $3c_3$ , see Table II).

Finally, we discuss the electron energy dispersions and density of states, which are calculated using the model described in Sect. III. First, we analyze the influence of the energy transfer (hopping) to the correlation gap. Fig. 9 shows the correlation gap  $\Delta_{corr}$  vs. the Anderson-Hubbard parameter  $U$ . The plotted curves are calculated using Eq.(5) and  $J = 4t^2/U=0.13 \text{ eV}$  for different hopping energy ratios  $t_{xy}/t$  and  $t_0/t$ . From Fig. 9 we conclude that the main influence to the correlation gap value comes from the Anderson-Hubbard parameter  $U$ . Because of that, by knowing the electronic gap from the ellipsometric or optical absorption measurements and the exchange energy  $J$  from the Raman spectroscopy we can determine the hopping parameters and the onsite electron-electron repulsion  $U$ . However, relative ratio of the hopping energies perpendicular and parallel to the legs as well as the interladder hopping, does not influence much the correlation gap. Namely, a decrease of the transfer energy along the rungs from  $t_0/t=1$  to  $t_0/t=0.5$  increases  $\Delta_{corr}$  for about 6%. Also, an increase of the interladder hopping  $t_{xy}$  from 0 to 10% of the hopping value  $t$  along the legs, produces a decrease of  $\Delta_{corr}$  for about 2.5%. Therefore, the interladder effects on electronic structure of  $\text{Sr}_{14}\text{Cu}_{24}\text{O}_{41}$  are found to be negligibly small even though the distance between the neighboring ladders is short (see Fig. 1). The correlation gap is observed at 1.4 eV. This value is determined as a maximum of dielectric function  $\epsilon_2(\omega)$  obtained from KKA of the unpolarized reflectivity data, see Inset (b) of Fig. 3(b). Using this value and the fact that  $t_0/t = 1$  (comes from  $J_0/J = 1$ ),  $t_{xy} = 0$  we obtained  $U=2.1 \text{ eV}$ . Similar values for the correlation gap and  $U$  has been also found in  $\text{SrCuO}_2$  [34].

Energy dispersion, shown in Inset of Fig. 2, allows us to assign the 1.86 eV peak in Fig. 3(a) to the gap value ( $\Delta_1=1.87 \text{ eV}$ ) between bonding and antibonding bands at the Z-point. Also, 2.4 eV peak from the ellipsometric measurements corresponds to the gap from the lowest occupied band ( $L_6$ , Fig. 2) to the highest empty band at Z-point of Brillouine zone ( $\Delta_2=2.4 \text{ eV}$ ). By comparison of our measured and calculated gap values, with previously published results [17, 35], we found that our  $t_0/t$  ratio is close to the ratio determined in [17]. Mizuno *et al.*, [35], calculated the optical conductivity for small clusters, simulating the ladders and the chains. They obtained the gap for the ladder at about 1.7 eV while the contribution from the chains mainly emerges at a higher energy showing the large spectral weight at around 2.6 eV. These values are very close to our experimental results. Therefore,

the peaks at 1.86, 2.4 and 2.5 eV, see Fig. 3(b), may correspond to the ladders and the chains, respectively.

In conclusion, we studied the optical properties of the  $\text{Sr}_{14}\text{Cu}_{24}\text{O}_{41}$  single crystal. The lattice vibrations are analyzed using the far-infrared reflectivity and Raman scattering measurements in the wide frequency and temperature range. At temperatures below 150 K the new IR and Raman modes appear, presumably due to the charge ordering. The two-magnon excitations are found in the Raman spectra which could be related to minimal ( $2\Delta$ ) and maximal (twice the top of the magnon brunch) magnon energy. The exchange constants along the legs and rungs of the ladders are found to be the same,  $J = J_0 \sim 120$  meV. The optical reflectivity and the ellipsometric measurements are used to study the charge dynamics. The gap values of 1.4 eV, 1.86 eV (2.5 eV) for the ladders (chains) along the **c**-axis and 2.4 eV along the **a**-axis are found. These results are analyzed using tight-binding approach for the correlated electrons. The correlation gap value of 1.4 eV is calculated with the transfer energy (hopping) parameters  $t=t_0=0.26$  eV, along and perpendicular to the legs, and  $U=2.1$  eV, as a Coulomb repulsion.

## VI. ACKNOWLEDGMENT

We thank W. König for low-temperature infrared measurements. Z.V.P., V.A.I and O.P.K acknowledge support from the Research Council of the K.U. Leuven and DWTC. The work at the K.U. Leuven is supported by the Belgian IUAP and Flemish FWO and GOA Programs. M.J.K thanks Roman Herzog - AvH for partial financial support.

- 
- [1] E. M. Mc.Carron, M. A. Subramanian, J. C. Calabrese, and R. L. Harlow, *Mat. Res. Bull.* **23**, 1355 (1988).
- [2] M. Uehara, T. Nagata, J. Akimitsu, H. Takahashi, N. Mori, and K. Kinoshita, *J. Phys. Soc. Jpn.* **65**, 2764 (1996).
- [3] N. Motoyama, T. Osafune, T. Kakeshita, H. Eisaki, and S. Uchida, *Phys. Rev. B* **55**, R3386 (1997).
- [4] S. A. Carter, B. Batlogg, R. J. Cava, J. J. Krajewski, W. F. Peck, Jr, and T. M. Rice, *Phys. Rev. Lett.* **77**, 1378 (1996).
- [5] Z. Hiroi, S. Amelinckx, G. Van Tendeloo, and N. Kobayashi, *Phys. Rev. B* **54**, 15849 (1996).
- [6] T. Imai, K. R. Thurber, K. M. Shen, A. W. Hunt, and F. C. Chou, *Phys. Rev. Lett.* **81**, 220 (1998).
- [7] M. Takigawa, N. Motoyama, H. Eisaki, and S. Uchida, *Phys. Rev. B* **57**, 1124 (1998).
- [8] R. S. Eccleston, M. Uehara, J. Akimitsu, H. Eisaki, N. Motoyama, and S. Uchida, *Phys. Rev. Lett.* **81**, 1702 (1998).
- [9] M. Matsuda, K. Katsumata, H. Eisaki, N. Motoyama, S. Uchida, S. M. Shapiro, and G. Shirane, *Phys. Rev. B* **54**, 12199 (1996).
- [10] T. Takahashi, T. Yokoya, A. Ashihara, O. Akaki, H. Fujisawa, A. Chainani, M. Uehara, T. Nagata, J. Akimitsu and H. Tsunetsuga, *Phys. Rev. B* **56**, 7870 (1997).
- [11] D. E. Cox, T. Iglesias, K. Hirota, G. Shirane, M. Matsuda, N. Motoyama, H. Eisaki, and S. Uchida, *Phys. Rev. B* **57**, 10750 (1998).
- [12] T. Osafune, N. Motoyama, H. Eisaki, and S. Uchida, *Phys. Rev. Lett.* **78**, 1980 (1997).
- [13] E. Dagotto, *Rep. Prog. Phys.* **62**, 1527 (1999).
- [14] M. V. Abrashev, C. Thomsen, and M. Surtchev, *Physica C* **280**, 297 (1997).
- [15] S. Sugai and M. Suzuki, *Phys. Stat. Sol. (b)* **215**, 653 (1999).
- [16] V. A. Ivanov, *J. Phys.: Cond. Matter* **6**, 2065 (1994).
- [17] S. Koike, K. Yamaji and T. Yanagisawa, *J. Phys. Soc. Jpn.* **68**, 1657 (1999).
- [18] V. A. Ivanov, *Physica B* **186-188**, 921 (1993).
- [19] V. A. Ivanov, K. Yukushi, E. Ugolkova, *Physica C* **275**, 26 (1997).
- [20] D. E. Aspnes, *J. Opt. Soc. Am.* **70**, 1275 (1980).

- [21] D. L. Rousseau, R. P. Bauman, and S. P. S. Porto, *J. Raman Spectrosc.* **10**, 253 (1980).
- [22] M. V. Abrashev, A. P. Litvinchuk, C. Thomsen, and V. N. Popov, *Phys. Rev. B* **55**, 9136 (1997).
- [23] E. T. Hayen, R. Liu, C. Thomsen, R. Kremer, M. Cardona, J. Karpinski, E. Kaldis, and S. Rusiecki, *Phys. Rev. B* **41**, 11058 (1990).
- [24] G. Kliche and Z. V. Popović, *Phys. Rev. B* **42**, 10060 (1990).
- [25] Z. V. Popović, S. D. Dević, V. N. Popov, G. Dhahlenne and A. Revcolevschi, *Phys. Rev. B* **52**, 4185 (1995).
- [26] E. T. Heyen, J. Kircher, and M. Cardona, *Phys. Rev. B* **45**, 3037 (1992).
- [27] Y. Tokura, S. Koshihara, T. Arima, H. Takagi, S. Ishibashi, T. Ido, and S. Uchida, *Phys. Rev. B* **41**, 11657 (1990).
- [28] S. Tsuji, K. Kumagai, M. Kato and Y. Koike, *J. Phys. Soc. Jpn.* **65**, 3474 (1996).
- [29] M.J.Konstantinović Z. V. Popović, M. Isobe and Y. Ueda, cond-mat/0001168 preprint.
- [30] R. Liu, M. V. Klein, D. Salamon, S. L. Cooper, W. C. Lee, S. W. Cheong, and D. M. Ginsberg, *J. Phys. Chem. Solids* **54**, 1347 (1993).
- [31] S. Sugai, T. Shinoda, N. Kobayashi, Z. Hiroi and M. Takano, *Phys.Rev.* **B 60**, R6969 (1999).
- [32] M. Matsuda, K. Katsumata, R. Eccleston, S. Brehmer and H.J. Mikeska, 1999. Preprint as discussed in Ref.[13]
- [33] T. Barnes, E. Dagotto, J. Riera, and E.S. Swanson, *Phys. Rev. B* **47**, 3196 (1993).
- [34] Z. V. Popovic et al, unpublished
- [35] Y. Mizuno, T. Tahoyama and S. Maekawa, *J. Phys. Soc. Jpn.* **66**, 937 (1997).



FIG. 1: Schematic representation of the  $\text{Sr}_{14}\text{Cu}_{24}\text{O}_{41}$  crystal structure in the (a) (010) and (b) (001) plane.

FIG. 2: The electron density of states as a function of dimensionless energies  $\xi/2t$ . Inset: The tight-binding dispersions for correlated electrons in  $\text{Sr}_{14}\text{Cu}_{24}\text{O}_{41}$  with parameters  $t=t_0=0.26$  eV,  $t_{xy}=0.026$  eV. The momenta are given in units  $|p_x\sqrt{2}|=|p_z|=\pi$  of the Brillouine zone boundaries, the Fermi energy  $E_F = 0$  is inside of the correlation gap.

FIG. 3: Room temperature imaginary part ( $\epsilon_2$ ) of the pseudodielectric function of  $\text{Sr}_{14}\text{Cu}_{24}\text{O}_{41}$ . The spectra of the (010) surface taken with a) a-axis, b) c-axis, parallel to the plane of incidence. Inset: (a) Reflectivity spectra obtained by calculation using  $\epsilon_1$  and  $\epsilon_2$ ; (b) unpolarized reflectivity spectrum measured at room temperature.

FIG. 4: Room temperature polarized far-infrared reflectivity spectra of  $\text{Sr}_{14}\text{Cu}_{24}\text{O}_{41}$  single crystal for (a) the  $\mathbf{E}||\mathbf{a}$  and (b) the  $\mathbf{E}||\mathbf{c}$  polarizations. The experimental values are given by the open circles. The solid lines represent the calculated spectra obtained by fitting procedure described in the text.

FIG. 5: Temperature dependent Raman scattering spectra for (aa) polarized (a) and (cc) polarized (b)-(g) configurations.  $\lambda_L = 514.5$  nm.

FIG. 6: Raman spectra measured at  $T=8$  K in the  $700\text{-}3300$   $\text{cm}^{-1}$  spectral range.

FIG. 7: Frequency and intensity dependencies of the two-magnon mode at about  $2840$   $\text{cm}^{-1}$  as a function of temperature.

FIG. 8: (a) The (cc) polarized Raman spectra measured at  $T=10$  K with  $647.1$  and  $488$  nm excitation lines. (b) Polarized far-infrared reflectivity spectra measured at  $T=10$  K for  $E||c$  (b) and  $E||a$  (c) polarizations. Dielectric functions  $\epsilon_2(\omega)$  and  $-Im[1/\epsilon(\omega)]$  are obtained using KKA of reflectivity data.

FIG. 9: The correlation gap vs. U parameter dependence for different transfer energy ratios.

TABLE I: Oscillator fit parameters (in  $\text{cm}^{-1}$ ) of the reflectivity data,  $T=300$  K.

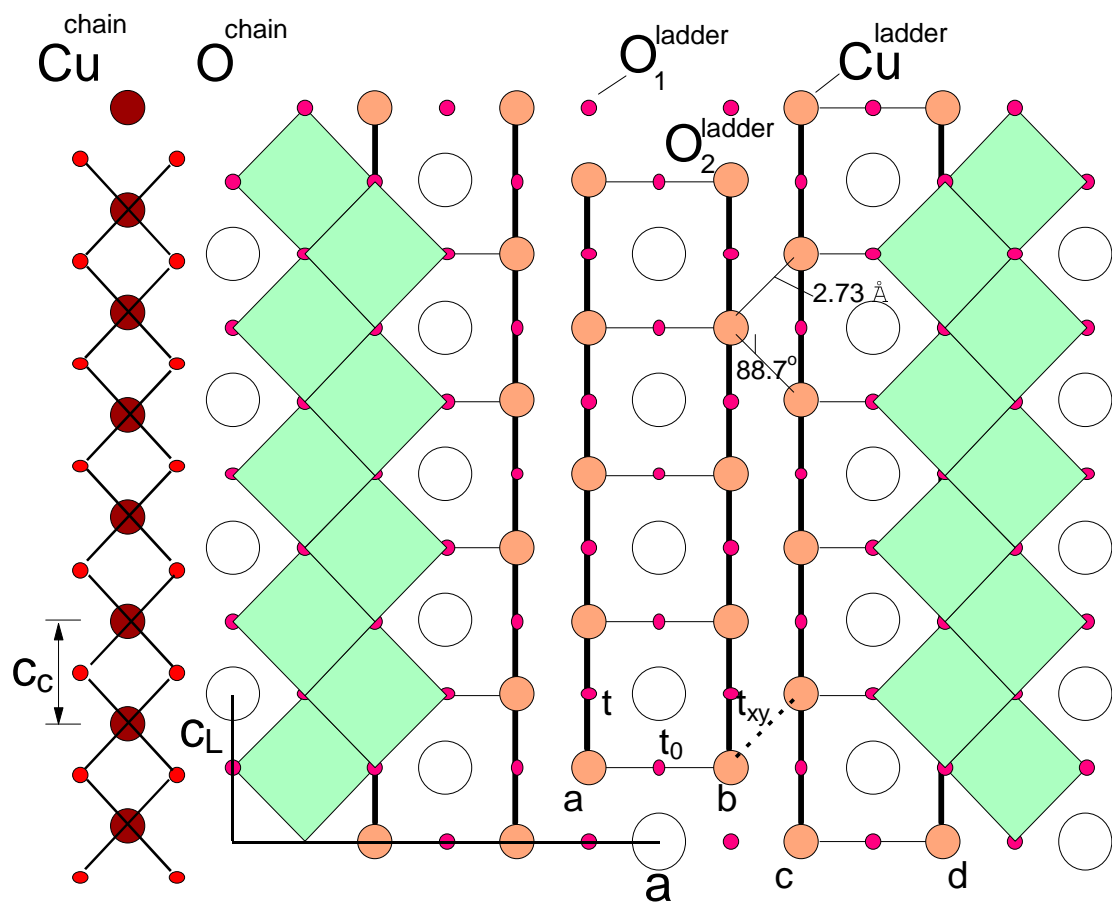
Polarization	$\omega_{TO}$	$\gamma_{TO}$	$\omega_{LO}$	$\gamma_{LO}$	$\omega_p$	$\tau^{-1}$	$\epsilon_\infty$
	164	6	164.6	5.5			
	194	6	210	14			
	219	10	223	10			
	249	14	250	14			
<b>E    a</b>	283.5	14	284	14	1000	4000	4.8
	310.4	8	311	8			
	554	16	585	28			
	623	19	676	22			
	135	6	140	10			
	148	5	150	5			
	253	12	257	17			
	293	18	300	14			
<b>E    c</b>	345	26	364	10	4000	18200	4
	486	20	502	20			
	540	25	568	17			
	596	20	600	17			
	620	30	629	14			

TABLE II: Frequencies (in  $\text{cm}^{-1}$ ) of Raman active modes measured at  $T=8$  K with  $\lambda_L=488$  nm, 514.5 nm and 647.1 nm, (Figs. 5(g) and 8(a)). By \* we denoted the modes influenced by charge ordering.

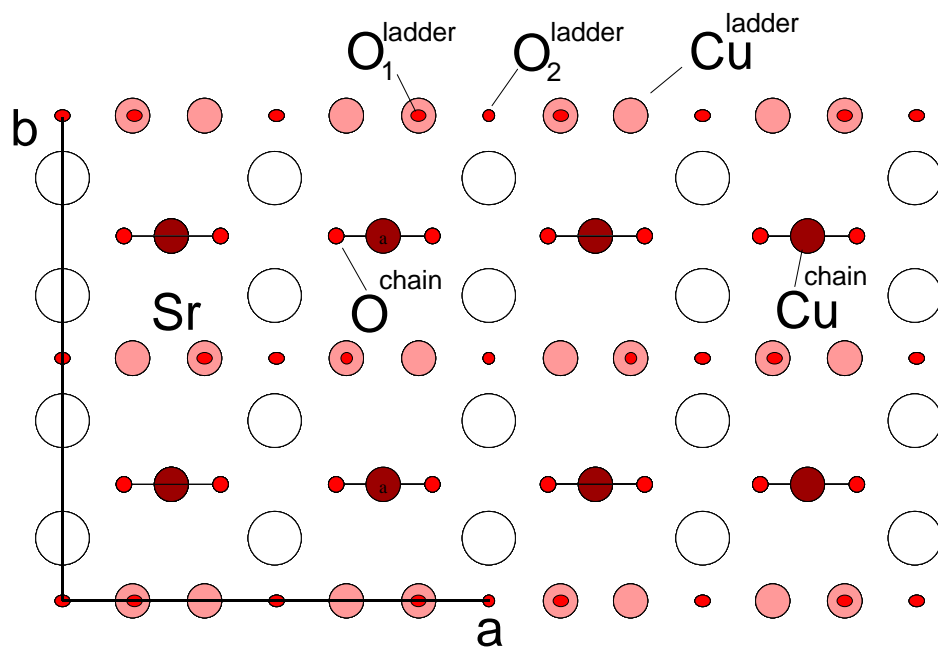
488 nm	514.5 nm	647.1 nm	Remark
-	-	115	-
154	-	153	$a_1$
197	-	-	-
208	213*	208	$a_2$
224	224	223	-
-	-	230	-
-	237*	238	-
251	254	-	-
-	265*	-	-
-	268*	-	-
-	293*	-	-
304	304	-	-
-	316	316	$a_3$
-	-	359	$c_1$
-	-	381	-
500	497*	496	$c_2$
-	516*	-	-
532	535*	-	-
553	556	-	-
-	568*	568	$c_3$
586	585	585	$a_4$
632	630	-	-
-	-	652	$a_5$

TABLE III: Mode frequencies (in  $\text{cm}^{-1}$ ) observed in Raman spectra measured with  $\lambda_L=647.1$  nm, Fig.6(a).

No. of peaks	Frequency	Remark
1	735	$a_1 + a_4$
2	758	-
3	805	$a_1 + a_5$
4	860	$a_2 + a_5$
5	946	$c_1 + a_4$
6	1005	$c_1 + a_5$
7	1069	$c_2 + c_3$
8	1152	$c_2 + a_5$
9	1164	$2a_4$
10	1132	$a_4 + a_5$
11	1300	$2a_5$



(a)



(b)

